

3D in-situ profiling in a laser micromachining station using dual-comb LiDAR

Hayk Soghomonyan,¹ Justinas Pupeikis,^{1,2} Benjamin Willenberg,^{1,2} Armin Stumpp,³ Lukas Lang,^{1,2} Christopher R. Phillips,¹ Bojan Resan,³ and Ursula Keller¹

¹*Department of Physics, Institute for Quantum Electronics, ETH Zurich, 8093 Zurich, Switzerland*

²*K2 Photonics AG, Hardturmstrasse 161, 8005 Zurich, Switzerland*

³*School of Engineering, University of Applied Sciences and Arts Northwestern Switzerland, Klosterzelgstrasse 2, 5210 Windisch, Switzerland*

(*Electronic mail: hayks@phys.ethz.ch)

(Dated: 15 April 2025)

We demonstrate the integration of coaxial dual-comb LiDAR into a laser micromachining station, enabling 3D profiling with sub-micron axial precision without moving the machined piece. This setup facilitates in-situ nondestructive testing (NDT) and evaluation, reducing the effort and time required for micromachining process development and control.

This article has been submitted to the Journal of Applied Physics.

I. INTRODUCTION

Laser micromachining has emerged as the key technique for producing high-precision components for industries such as consumer electronics, medical, watch and jewelry, automotive, aerospace, and defense^{1–3}. However, the development and qualification of suitable micromachining processes remain time-intensive and require significant expertise^{4–6}. Development typically involves multiple iterations of micromachining a part, followed by inspection with an external device, such as a laser scanning microscope or a white light interferometer. This workflow necessitates moving and remounting parts for inspection, which degrades precision, repeatability, and prolongs qualification times. Moreover, even established processes can fail due to variations in material properties or machining laser performance, necessitating re-qualification. The integration of in-situ non-destructive testing (NDT) and evaluation is crucial for establishing an active feedback loop that ensures the achievement of the desired 3D profile, irrespective of variations in sample or machining laser quality. In addition, in-situ profiling could open opportunities for machine learning deployment in the micromachining process, which could translate into significant time savings for the end users. One approach is to incorporate an optical coherence tomography (OCT) system into the micromachining station, as demonstrated in previous reports^{7–10}. Both spectral-domain OCT (SD-OCT) and swept-source OCT (SS-OCT) offer excellent performance that has led to their widespread deployment, especially in ophthalmology¹¹. However, high-resolution OCT systems are expensive and would require significant customization to meet precision (sub-micrometer), measurement depth (millimeter to centimeter scale), wavelength (close to the machining laser) and integration constraints applicable for deployment in laser materials processing workstations^{7–10}.

White-light interferometry (WLI) is also a suitable tech-

nique. However, the need for mechanical delay scanning may not be compatible with the rapid beam scanners typically employed in micromachining. Additional significant integration challenges emerge because the reference path needs to be introduced, and optical delay over large distances, typically tens to hundreds of centimeters, needs to match, which is sensitive to environmental drifts. The frequency comb-based WLI¹² overcomes the range limitations of incoherent light sources, but still involves mechanical scanning.

Here, we demonstrate an alternative approach utilizing the emerging dual-comb ranging technique^{13,14}, which has compelling advantages such as high precision, long working range, and rapid optical delay scanning, especially when utilizing gigahertz dual optical frequency combs^{13,15–19}. The use of a shared laser cavity arrangement also helps reduce noise^{15,20} and enables a compact and cost-effective footprint^{15,21}.

In contrast to commonly used SD-OCT²², dual-comb ranging is a time-domain measurement, which means that only a single photodiode is enough to obtain the necessary ranging information. The time-domain signal may be processed using various methods, which include digital processing with Hilbert transform¹⁴, or alternatively, it can be processed directly in the time-domain with cost-effective time-to-digital converter (TDCs) chips developed for LiDAR applications, or similar approaches²³. In contrast to WLI, dual-comb ranging offers motion-free and very rapid optical delay sweeps between the reference and probe arms, equivalent to more than 10 km/s. Such high-speed delay scanning is compatible with the rapid motion of the beam scanners. This particularly becomes true when 1-GHz or higher pulse repetition rate dual-comb lasers are employed, as they are directly compatible with optical delay sweeps in 10-100 kHz, while still satisfying the aliasing condition necessary for interferogram sampling.

In this paper, we explore 3D profiling using a prototyped 1-GHz single-cavity dual-comb laser. To leverage the coherence of the two pulse trains, we perform heterodyne beating between the scattered light from the sample and the reference to obtain coherent signal amplification, which then allows for high measurement dynamic range. The signals are digitized

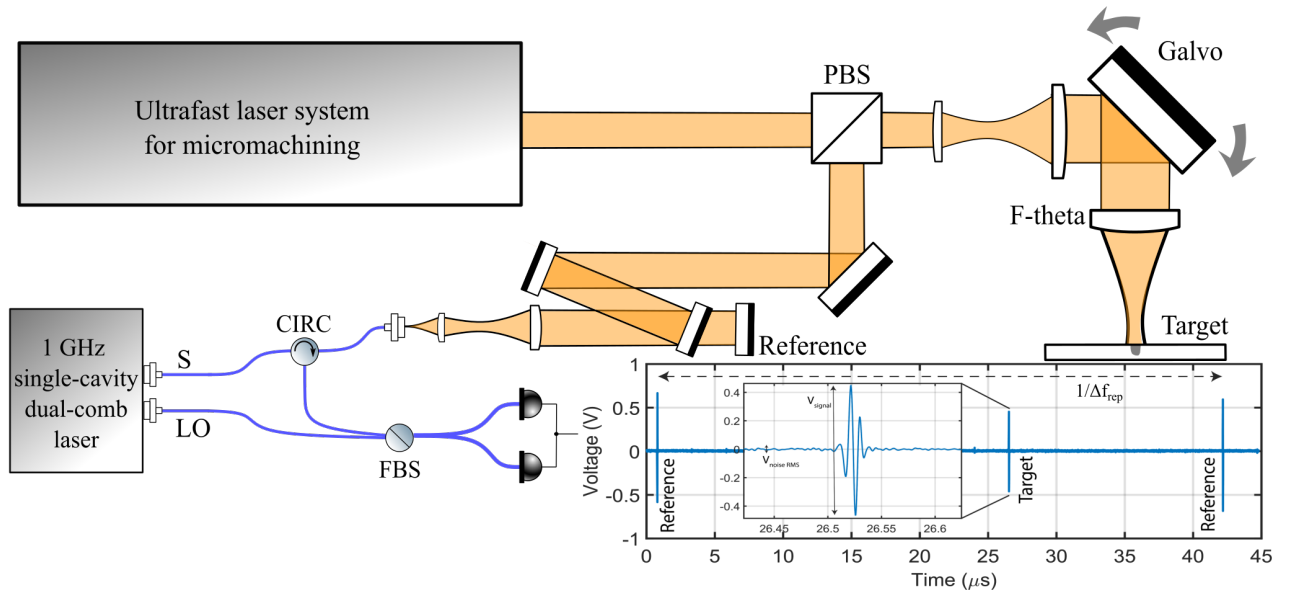


FIG. 1. Experimental setup. S – signal, LO – local oscillator, CIRC – circulator, FBS – fiber beam splitter, PBS – polarizing beam splitter. Inset shows example dual-comb LiDAR signal.

and processed using digital signal processing methods. By leveraging the pulsed nature of the dual-comb laser, efficient for non-linear processes, such as supercontinuum generation, further enhancements in resolution and precision could be achieved²⁴.

II. EXPERIMENTAL SETUP

Fig. 1 shows our setup and a typical signal obtained for a single scanner position. We integrated a recently reported single-cavity dual-comb laser²⁵ operating at 1056 nm center wavelength, with 18 nm FWHM bandwidth and $f_{rep} = 1$ GHz laser repetition rate into a laser micromachining station. The same dual-comb laser was also employed for long-range dual-comb ranging¹⁹. For laser micromachining, we used a Duetto 1064 nm picosecond laser from Time-Bandwidth Products. Because of wavelength overlap, the two lasers were combined via polarization.

The coaxially combined laser beams are then sent into a beam scanning system (intelliSCAN14, SCANLAB), after which the beams are focused with a 100 mm focal length f-theta lens on the sample. In this configuration, the lateral resolution is limited by the aperture of the beam scanner. We estimate the focused mode size to be around 20 μm . The dual-comb laser light backscattered from the sample surface is collected and mixed with a local oscillator to coherently amplify the returning light. The measurement setup was estimated to be sensitive to sub-nW average power of returning light, while up to 60 mW have been sent towards the target indicating ranging sensitivity up to 77 dB. The interferograms were digitized with a 250 MS/s sampling card and acquisitions were triggered on the scanner motion. In this proof-of-concept demonstration, the data was processed offline, but the

data acquisition card used is compatible with real-time signal processing as we have previously reported in the context of dual-comb range tracking application with the dual-comb laser used here¹⁹.

III. EXPERIMENTAL RESULTS

The sample was profiled in-situ using dual-comb LiDAR at three different stages: prior to machining, during machining, and after machining. The scan utilized a 550 x 300 point grid with a pixel spacing of 10 μm at $\Delta f_{rep} = 6.6$ kHz repetition rate difference between the two combs, which determined the effective update rate and corresponds to a single measurement acquisition time of 152 μs . The measurement speed was constrained by the bandwidth of the sampling card. A higher Δf_{rep} results in a broader spectrum of the dual-comb LiDAR signal with frequencies above the 125 MHz limit that can be digitized without aliasing at the 250 MS/s sampling rate. The entire profile scan, including surface scanning and the acquisition of five clean measurements at each lateral position, took approximately three minutes.

Fig. 2a illustrates the depth profile obtained at the conclusion of the machining process. For comparison, the same part was subsequently profiled using an external Laser Scanning Microscope (LSM) (Fig. 2b). We used LSM from Keyence, VK-X130K with a 10-x magnification objective, providing a total 240-x magnification.

A representative cross section of the sample profile before and during machining is shown in Fig. 2c. The depth profile obtained using the dual-comb LiDAR setup aligns closely with the LSM results, with a slight advantage in measuring high-aspect ratio holes. Dual-comb ranging can be considered part of a broader framework of Coherence Scanning Interfer-

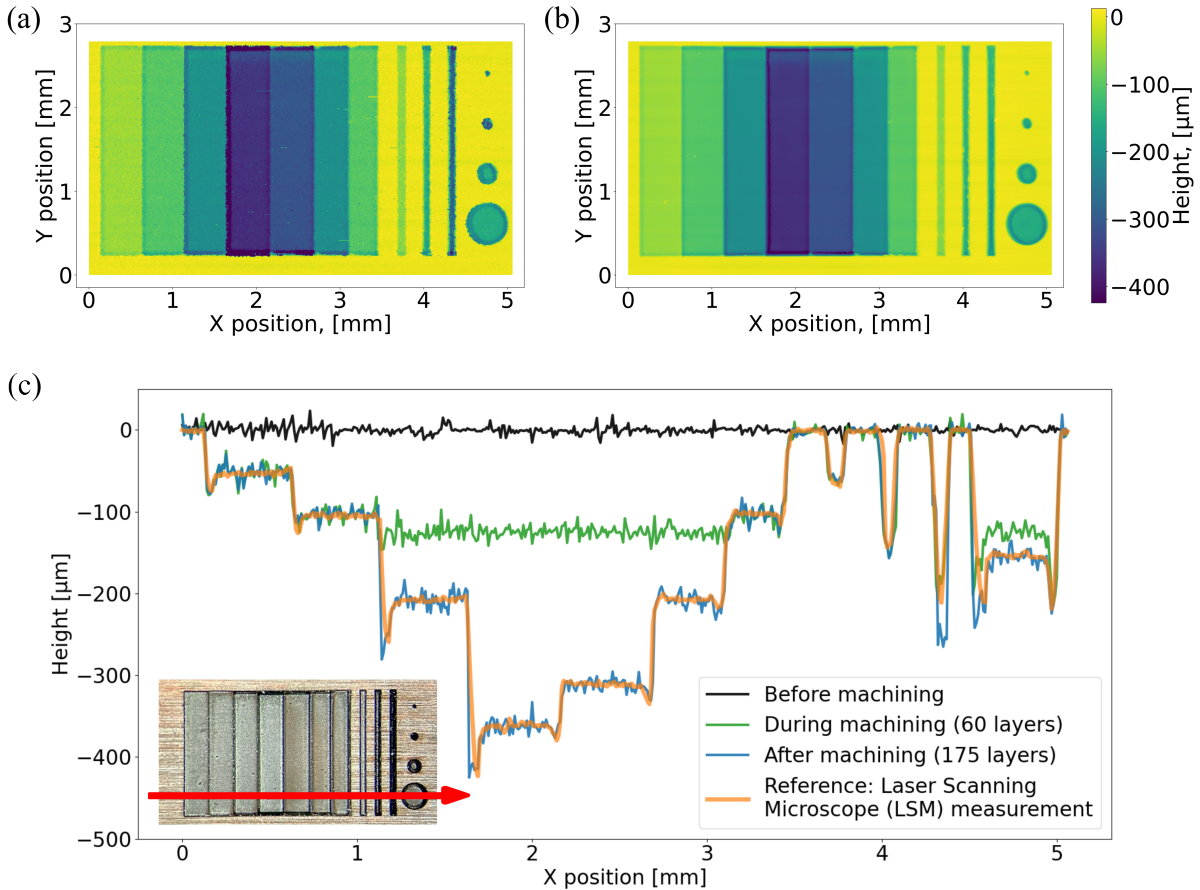


FIG. 2. 3D profile of laser micromachined part: (a) measured in-situ with dual-comb ranging, (b) measured with external laser scanning confocal microscope. (c) Example cross-section of the 3D profiles along the red arrow, including prior, during and after the machining process.

ometry (CSI) techniques that use interferometric ranging for surface profiling. CSI techniques are known for their compatibility with high-aspect ratio structures²⁶.

Moreover, the surface smoothness of the measurement results differs noticeably between the two methods, with the dual-comb LiDAR scan exhibiting stronger fluctuations. These fluctuations are partially attributed to speckle-induced errors, which will be discussed in a later section. However, the apparent difference in surface smoothness between the two methods is further amplified by the way the LSM measurement was processed. The LSM measurement in Fig. 2b was performed over multiple sections separately at a high transverse resolution. By the default settings of the LSM software the sections were consequently stitched together, and an averaging in the transverse direction was performed to get a scan at the final output resolution. This artificially smoothens the surface and makes the contrast between the two scans appear more extreme.

Another sample with a pre-machined double sine wave profile featuring steep surface angles was scanned to further evaluate the system's capabilities. The scan, represented in Fig. 3, was conducted with a resolution of 100 points per millimeter. Fig. 3a) shows an overview of this profile, while b) and c)

present cross-sections in the y-direction along the highest and lowest points, respectively.

Developing an optimal laser micromachining process for this microstructure required iterative refinement, alternating between the laser machine and an inspection tool like the LSM. Such iterative optimization processes are common in industrial micromachining but can be labor-intensive. In-situ diagnostics offer a means to periodically measure the ablation depth during the fabrication process while preserving the position and referencing of the workpiece, thereby enabling much more efficient and effective optimization of the process. Our dual-comb ranging setup is compatible with such in-situ measurements.

Before the main experiment described above, as a first evaluation of the dual-comb LiDAR precision, we collected 100 measurements per lateral position on a non-cooperative stationary target. Here we collected the data using a 5 GS/s oscilloscope and could set a higher $\Delta f_{rep} = 20$ kHz resulting in a 50 μ s acquisition time per measurement. The standard deviation of the distance measurements was used as an uncertainty metric, yielding an average uncertainty of 680 nm across all lateral positions, without averaging multiple measurements per position. As expected in the absence of drifts,

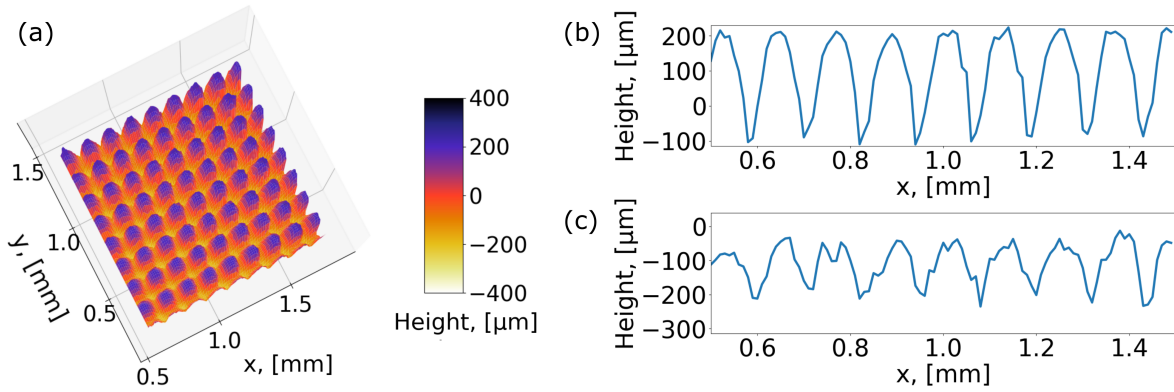


FIG. 3. a) LiDAR measurement of a machined double-sine wave profile, b) Cross-section along the peaks, c) Cross-section along the valleys.

the depth measurement precision scales with the square root of the number of averages per lateral position. In case of 5 averages it reached a 310 nm average standard deviation and for 10 averages 220 nm. Based on this, we decided to take five measurements per point for the samples in Fig. 2 and Fig. 3 to obtain a higher precision. As discussed in the next section, the single point measurement uncertainty in these profile measurements is indeed in sub- μm range, however the final precision is limited by the speckle effect caused by a rough surface.

In another experiment using the same dual-comb laser, a single measurement time-of-flight precision of 100 nm was demonstrated at a long range with a cooperative (highly reflective) target at a 5-kHz update rate¹⁹.

IV. DISCUSSION

One apparent feature of the LiDAR measurements in Fig. 2c is the relatively strong fluctuation of the measured profile compared to the expected precision. The theoretically achievable precision of the system depends on the signal-to-noise ratio (SNR) and is limited by the Cramer-Rao Lower Bound, with a single measurement standard deviation given by²⁷

$$\delta = \frac{c}{2 \cdot B \cdot \sqrt{2 \cdot SNR}} \quad (1)$$

A FWHM optical bandwidth of $B = 4.84$ THz results in an estimated lower bound for a single point measurement uncertainty of $\delta = \frac{21.9}{\sqrt{SNR}}$ μm . Here, the SNR is defined for time-domain signal power:

$$SNR = \frac{V_{pp}^2}{V_{noise}^2} \quad (2)$$

where V_{pp} is the peak-to-peak voltage and V_{noise} is the rms noise voltage.

With a mean SNR of 1000 observed for the machined surface measurement, the lower bound for single point measurement uncertainty is 0.69 μm . For each lateral position on the

surface, five measurements were collected and their standard deviation was calculated. The standard deviations of these single point measurements, averaged over each machined section (1 to 7) in Fig. 4, range from 0.7 to 0.85 μm , closely approaching the estimated lower bound.

Based on the demonstrated sub-micrometer single point measurement precision of the system, we conclude that the transverse fluctuations in the measured profile are a consequence of surface roughness and not due to statistical uncertainty in single point measurements. The measurement is influenced by the surface roughness in two ways: (1) the surface is not smooth, so true fluctuations of the surface profile are expected, and (2) there is a contribution from the speckle effect introducing an additional error caused by the distortion of the signal reflected from a rough surface.

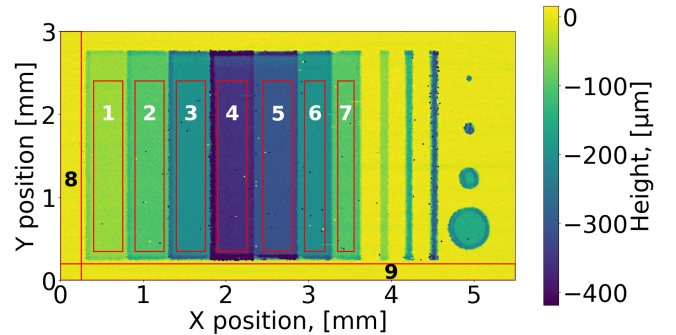


FIG. 4. Nine sections of the machined profile where the surface roughness was analyzed.

A. Estimation of Surface Roughness and Speckle Induced Uncertainty

In any coherent laser-ranging method, high spatial frequency surface roughness can impact precision. A finite spot size of the beam at the measurement point means that a rough surface cannot always be laterally resolved. With coherent il-

lumination of the sample, the photodiode samples a portion of the speckle pattern originating from interference between multiple reflections within the illuminated region. This interference introduces additional uncertainty in the measured depth.

The relation between surface roughness and measurement precision has been studied extensively in previous works^{28–31}. The analytical result using first order statistics is:

$$\delta z = \frac{1}{\sqrt{2}} \sqrt{\frac{1}{r}} \sigma_h \quad (3)$$

where σ_h is the rms surface roughness, and

$$r = \frac{I}{\langle I \rangle} \quad (4)$$

is the ratio of the individual speckle intensity I to the mean intensity of the speckle field $\langle I \rangle$ of a rough planar surface.

We estimate the distribution of r for the speckle field using V_{pp}^2 of the measured photodiode signal. Using this in combination with the eq. 3 we can calculate the ratio:

$$\alpha = \langle \delta z \rangle / \sigma_h \quad (5)$$

between the expectation value of the speckle-induced uncertainty $\langle \delta z \rangle$ and σ_h (see the appendix). This has been done for different machined (sections 1-7) and non-machined (sections 8 and 9) planar sections shown in Fig. 4. Because there is no statistical dependence between the true position and the measurement error of a single point we can approximate the variance of the height distribution of a measured planar profile as:

$$\sigma_z^2 = \sigma_h^2 + \langle \delta z \rangle^2 \quad (6)$$

For each of the planar sections labeled 1-9 in Fig. 4 we calculated the variance σ_z of the measured height and estimated the ratio α (see the appendix). Using eq. 5 and 6 we calculate the expectation value of the measurement uncertainty $\langle \delta z \rangle$ and the rms surface roughness σ_h . The results are shown in the table below:

	Section								
	1	2	3	4	5	6	7	8	9
α	1.06	1.07	1.08	1.05	1.05	1.06	1.06	1.41	1.46
σ_z , [μm]	7.6	7.6	7.4	7.6	7.2	7.2	7.1	5.4	4.1
σ_h , [μm]	5.2	5.2	5.0	5.2	4.9	4.9	4.9	3.1	2.3
$\langle \delta z \rangle$, [μm]	5.5	5.6	5.4	5.5	5.2	5.2	5.2	4.4	3.4

TABLE I. rms surface roughness σ_h and expected speckle induced error $\langle \delta z \rangle$ estimations for sections 1-9 in Fig. 4

It is also possible to numerically estimate (see the appendix) the relation of speckle induced measurement uncertainty and the surface roughness shown in Fig. 5 for a more general case of coherent ranging using polychromatic light sources^{28,29}. We see that they are approximately on the same scale, which can also be observed in Table I.

The relation in Fig. 5 is derived for a Gaussian spectrum and the corresponding $1/e$ coherence length. In case of soliton pulses, a similar relation is expected, possibly with rescaled coherence length units because of a different spectral shape.

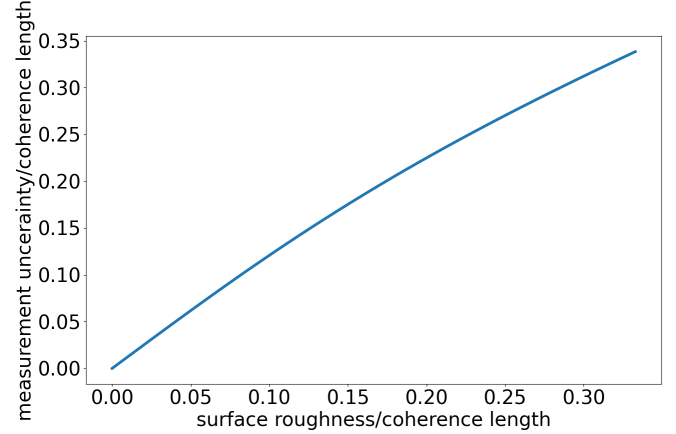


FIG. 5. Numerically calculated dependence of speckle induced measurement uncertainty from the surface roughness in units of the coherence length of the laser source.

B. System performance under reduced SNR conditions

The increased surface roughness from the machining process also reduces the reflectivity, thus influencing the measurement not only through the speckle effect but also through a reduced SNR value. Other factors can also reduce reflectivity, such as the redeposition of removed metal particles on the surface, oxidation of the surface, or other types of surface contamination. Still, even with reduced SNR, for most rough surfaces, the speckle effect remains the dominant source of error.

As shown in Fig. 6(a), the SNR of machined sections is significantly lower than that of non-machined sections. A mean SNR of 1000 was recorded for the machined sections, corresponding to a 10x–100x reduction in reflectivity. Despite this decrease, the system continues to function effectively with no significant limitations.

V. CONCLUSIONS

In conclusion, we have demonstrated the integration of coaxial dual-comb LiDAR into a laser micromachining station, enabling 3D profiling during the micromachining process. This integration facilitates in-situ non-destructive testing (NDT) and evaluation of machined parts, reducing the effort required for both process development and control. At $\Delta f_{rep} = 6.6$ kHz, a scan of 165000 lateral positions with five measurements at each was completed in three minutes, which can be further reduced by taking fewer measurements per

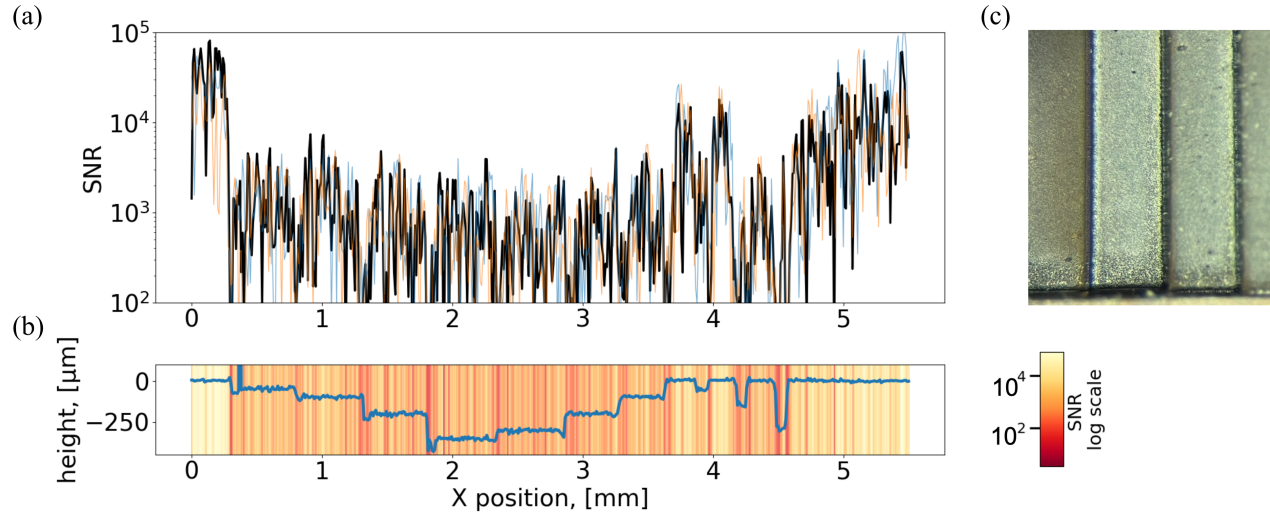


FIG. 6. (a) SNR along an example cross-section. (b) Measured height profile and SNR color map along the cross-section, matched with positions of (a), (c) Example of the machined surface with visible graining caused by a drift of the focus in case of an imperfect machining process.

point, increasing the acquisition rate, and optimizing the scanning of the surface. At a mean SNR of 1000 for machined surfaces, the standard deviation over multiple measurements of a single lateral position was $0.8 \mu\text{m}$. However, the precision is limited by the speckle induced error, which is on the same scale as the estimated surface roughness. This additional error was estimated to be $5.4 \mu\text{m}$ on average for the machined surfaces with an estimated rms surface roughness of $5.0 \mu\text{m}$.

Compared to confocal LSM, the dual-comb LiDAR offers slightly better capability in measuring high-aspect-ratio features. Additionally, unlike OCT techniques, it eliminates the need for reference arm delay matching, making it particularly suitable for profiling large parts ($\gg 1 \text{ cm}$). Beyond serving as a replacement for traditional 3D profilers, this technique can provide auxiliary functionalities such as autofocus of the machining laser on the sample and has the potential to enable active machining control. Practical implementation challenges include addressing optical isolation to protect the photodetector from high-power machining laser light and developing methods to combine different wavelengths within a single system to enable integration into a wider range of laser machining setups. These considerations will be crucial for the advancement of this technology toward broader industrial adoption. Future developments could explore the use of super-continuum generation to further enhance the performance of the LiDAR system²⁴. A broader bandwidth of hundreds of nm could potentially improve both resolution and precision more than 10 times, making the system particularly advantageous for applications such as machining depth control in in-glass machining. A better resolution would also make the system less susceptible to the speckle effect. In addition, integrating

hyperspectral imaging techniques could enable material layer differentiation. This combination of higher precision, resolution, and expanded functionality could significantly broaden the system's applicability, particularly in areas like semiconductor inspection.

FUNDING

This project has received funding from Innovation Booster Photonics under Grant Nr. IB-P 23.022.

ACKNOWLEDGMENTS

The authors thank S. L. Camenzind for useful discussions. The authors acknowledge experimental support from Matthias Julius.

CONFLICT OF INTEREST

LL, BW, and JP declare a partial employment with K2 Photonics.

DATA AVAILABILITY

Data underlying the results presented in this article are available in the ETH Zurich Research Collection Library.

- ¹B. N. Chichkov, C. Momma, S. Nolte, F. Alvensleben, and A. Tünnermann, “Femtosecond, picosecond and nanosecond laser ablation of solids,” *Applied Physics A* **63**, 109–115 (1996).
- ²B. Neuenschwander, G. F. Bucher, C. Nussbaum, B. Joss, M. Muralt, U. W. Hunziker, and P. Schuetz, “Processing of metals and dielectric materials with ps-laserpulses: results, strategies, limitations and needs,” in *Laser Applications in Microelectronic and Optoelectronic Manufacturing XV*, Vol. 7584, edited by H. Niino, M. Meunier, B. Gu, G. Hennig, and J. J. Dubowski, International Society for Optics and Photonics (SPIE, San Francisco, California, USA, 2010) p. 75840R.
- ³A. Schoonderbeek, V. Schütz, O. D.-I. Haupt, U. Stute, and L. Z. Hannover, “Laser processing of thin films for photovoltaic applications,” *Journal of Laser Micro Nanoengineering* **5**, 248–255 (2010).
- ⁴B. Neuenschwander, B. Jaeggi, M. Zimmermann, V. Markovic, B. Resan, K. Weingarten, R. de Loor, and L. Penning, “Laser surface structuring with 100 W of average power and sub-ps pulses,” *Journal of Laser Applications* **28**, 022506 (2016).
- ⁵F. Moglia, “New challenges for the laser micromachining community: How the minting industry and other application fields are motivating their supply chain in photonics to strive for even better performance,” *PhotonicsViews* **18**, 26–30 (2021).
- ⁶K. Yildirim, B. Nagarajan, T. Tjahjowidodo, and S. Castagne, “Development of a multi-sensor system for in-situ process monitoring of femtosecond laser micromachining,” *The International Journal of Advanced Manufacturing Technology* **135**, 799–813 (2024).
- ⁷D. Huang, E. A. Swanson, C. P. Lin, J. S. Schuman, W. G. Stinson, W. Chang, M. R. Hee, T. Flotte, K. Gregory, C. A. Puliafito, and J. G. Fujimoto, “Optical Coherence Tomography,” *Science* **254**, 1178–1181 (1991).
- ⁸O. Massow, M. Jackstadt, H. Wisweh, F. Will, and H. Lubatschowski, “OCT-aided femtosecond laser micromachining device,” in *Commercial and Biomedical Applications of Ultrafast Lasers IX*, Vol. 7203, edited by J. Neev, S. Nolte, A. Heisterkamp, and R. P. Trebino, International Society for Optics and Photonics (SPIE, San Jose, CA, 2009) p. 720307.
- ⁹M. Wiesner, J. Ihlemann, H. H. Müller, E. Lankenau, and G. Hüttmann, “Optical coherence tomography for process control of laser micromachining,” *Review of Scientific Instruments* **81**, 033705 (2010).
- ¹⁰C. Stehmar, M. Gipperich, M. Kogel-Hollacher, A. Velazquez Iturbide, and R. H. Schmitt, “Inline Optical Coherence Tomography for Multidirectional Process Monitoring in a Coaxial LMD-w Process,” *Applied Sciences* **12**, 2701 (2022).
- ¹¹M. Varghese, S. Varghese, and S. Preethi, “Revolutionizing medical imaging: a comprehensive review of optical coherence tomography (OCT),” *Journal of Optics* (2024), 10.1007/s12596-024-01765-6.
- ¹²P. Maslowski, K. F. Lee, A. C. Johansson, A. Khodabakhsh, G. Kowzan, L. Rutkowski, A. A. Mills, C. Mohr, J. Jiang, M. E. Fermann, and A. Foltynowicz, “Surpassing the path-limited resolution of Fourier-transform spectrometry with frequency combs,” *Physical Review A* **93**, 021802 (2016).
- ¹³S.-J. Lee, B. Widiyatmoko, M. Kourogi, and M. Ohtsu, “Ultrahigh Scanning Speed Optical Coherence Tomography Using Optical Frequency Comb Generators,” *Japanese Journal of Applied Physics* **40**, L878 (2001).
- ¹⁴I. Coddington, W. C. Swann, L. Nenadovic, and N. R. Newbury, “Rapid and precise absolute distance measurements at long range,” *Nature Photonics* **3**, 351–356 (2009).
- ¹⁵S. M. Link, A. Klenner, M. Mangold, C. A. Zaugg, M. Golling, B. W. Tilma, and U. Keller, “Dual-comb modelocked laser,” *Optics Express* **23**, 5521 (2015).
- ¹⁶K. J. Mohler, B. J. Bohn, M. Yan, G. Mélen, T. W. Hänsch, and N. Picqué, “Dual-comb coherent Raman spectroscopy with lasers of 1-GHz pulse repetition frequency,” *Optics Letters* **42**, 318 (2017).
- ¹⁷T. Voumard, J. Darvill, T. Wildi, M. Ludwig, C. Mohr, I. Hartl, and T. Herr, “1-GHz dual-comb spectrometer with high mutual coherence for fast and broadband measurements,” *Optics Letters* **47**, 1379 (2022).
- ¹⁸C. R. Phillips, B. Willenberg, A. Nussbaum-Lapping, F. Callegari, S. L. Camenzind, J. Pupeikis, and U. Keller, “Coherently averaged dual-comb spectroscopy with a low-noise and high-power free-running gigahertz dual-comb laser,” *Optics Express* **31**, 7103 (2023).
- ¹⁹S. L. Camenzind, L. Lang, B. Willenberg, J. Pupeikis, H. Soghomonyan, R. Presl, P. Ray, A. Wieser, U. Keller, and C. R. Phillips, “Long-Range and Dead-Zone-Free Dual-Comb Ranging for the Interferometric Tracking of Moving Targets,” *ACS Photonics* (2025), 10.1021/acsp Photonics.4c02199.
- ²⁰J. Pupeikis, B. Willenberg, S. L. Camenzind, A. Benayad, P. Camy, C. R. Phillips, and U. Keller, “Spatially multiplexed single-cavity dual-comb laser,” *Optica* **9**, 713 (2022).
- ²¹B. Willenberg, C. R. Phillips, J. Pupeikis, S. L. Camenzind, L. Liebermeister, R. B. Kohlhas, B. Globisch, and U. Keller, “THz-TDS with gigahertz Yb-based dual-comb lasers: noise analysis and mitigation strategies,” *Applied Optics* **63**, 4144 (2024).
- ²²M. Wojtkowski, R. Leitgeb, A. Kowalczyk, T. Bajraszewski, and A. F. Fercher, “In vivo human retinal imaging by Fourier domain optical coherence tomography,” *Journal of Biomedical Optics* **7**, 457 (2002).
- ²³H. Wright, J. Sun, D. McKendrick, N. Weston, and D. T. Reid, “Two-photon dual-comb LiDAR,” *Optics Express* **29**, 37037 (2021).
- ²⁴S. L. Camenzind, A. Nussbaum-Lapping, B. Willenberg, J. Pupeikis, J. Taher, T. Hakala, A. Kukko, J. Hyypää, P. Ray, C. R. Phillips, and U. Keller, “Broadband hyperspectral lidar with a free-running gigahertz dual-comb supercontinuum,” *Optics Letters* **50**, 1289–1292 (2025).
- ²⁵J. Pupeikis, H. Soghomonyan, B. Willenberg, L. Lang, C. R. Phillips, and U. Keller, “Ultra-low noise 1 GHz Yb:CaF₂ laser for dual-comb LiDAR,” in *Solid State Lasers XXXIII: Technology and Devices*, edited by W. A. Clarkson and R. K. Shori (SPIE, San Francisco, United States, 2024) p. 43.
- ²⁶J. Ma, X. Huo, J. Zhang, X. Fan, Z. Xu, W. Qiao, Y. Li, Y. Wang, D. Zhu, Z. Guo, Q. Yuan, and Z. Gao, “Topography reconstruction of high aspect ratio silicon trench array via near-infrared coherence scanning interferometry,” *Optics Express* **32**, 22493 (2024).
- ²⁷S. M. Kay, *Fundamentals of statistical signal processing*, Prentice Hall signal processing series (Prentice-Hall PTR, Englewood Cliffs, N.J., 1993) Chap. 3.11, pp. 53–58.
- ²⁸G. Parry, *Laser Speckle and Related Phenomena*, edited by J. C. Dainty, Topics in Applied Physics, Vol. 9 (Springer Berlin Heidelberg, Berlin, Heidelberg, 1975) Chap. 3.1, pp. 78–102.
- ²⁹P. Pavliček and J. Soubusta, “Theoretical measurement uncertainty of white-light interferometry on rough surfaces,” *Applied Optics* **42**, 1809 (2003).
- ³⁰P. Pavliček and O. Hýbl, “White-light interferometry on rough surfaces—measurement uncertainty caused by surface roughness,” *Applied Optics* **47**, 2941 (2008).
- ³¹E. Baumann, J.-D. Deschênes, F. R. Giorgetta, W. C. Swann, I. Coddington, and N. R. Newbury, “Speckle phase noise in coherent laser ranging: fundamental precision limitations,” *Optics Letters* **39**, 4776 (2014).

Appendix: 3D in-situ profiling in a laser micromachining station using dual-comb LiDAR

Hayk Soghomonyan,¹ Justinas Pupeikis,^{1,2} Benjamin Willenberg,^{1,2} Armin Stumpp,³ Lukas Lang,^{1,2} Christopher R. Phillips,¹ Bojan Resan,³ and Ursula Keller¹

¹Department of Physics, Institute for Quantum Electronics, ETH Zurich, 8093 Zurich, Switzerland

²K2 Photonics AG, Hardturmstrasse 161, 8005 Zurich, Switzerland

³School of Engineering, University of Applied Sciences and Arts Northwestern Switzerland, Klosterzelgstrasse 2, 5210 Windisch, Switzerland

(*Electronic mail: hayks@phys.ethz.ch)

(Dated: 15 April 2025)

A. Estimation of Surface Roughness and Speckle Induced Uncertainty

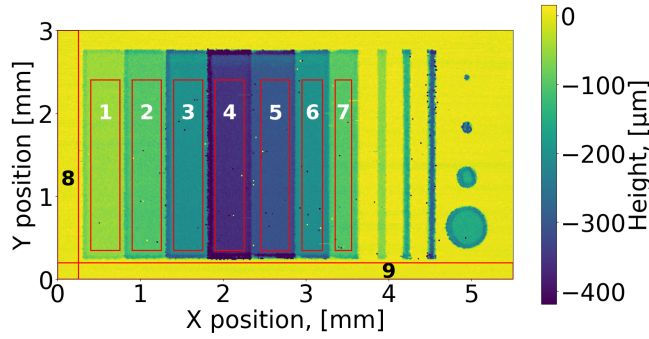


FIG. 1: Nine sections of the machined profile where the surface roughness was analyzed.

In any coherent laser-ranging method, high spatial frequency surface roughness can impact precision. A finite spot size of the beam at the measurement point means that a rough surface cannot always be laterally resolved. With coherent illumination of the sample, the photodiode samples a portion of the speckle pattern originating from interference between multiple reflections within the illuminated region. This interference introduces additional uncertainty in the measured depth.

This contribution of the speckle effect to the measurement uncertainty of coherent ranging methods has been studied in multiple works¹⁻⁴, based on analytical derivations and numerical simulations. Many approaches use first-order statistics to estimate the uncertainty of a range measurement for one single speckle:

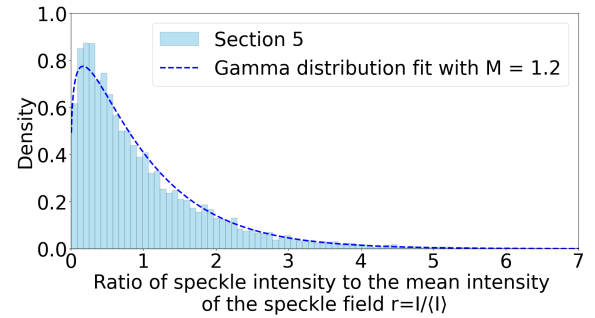
$$\delta z = \frac{1}{\sqrt{2}} \sqrt{\frac{\langle I \rangle}{I}} \sigma_h \quad (1)$$

Here σ_h is the rms surface roughness, I is the intensity of the captured light from a single speckle and $\langle I \rangle$ the average over the whole speckle field of a planar rough surface. The speckle induced uncertainty δz of a single measurement scales

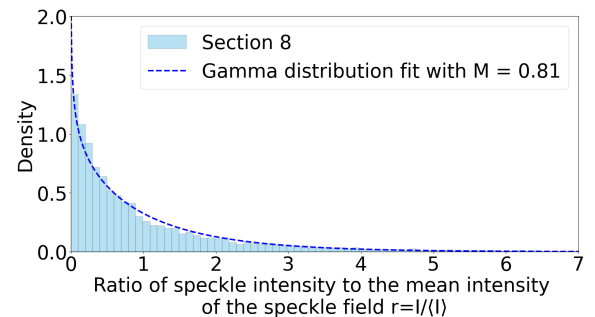
linearly with the surface roughness σ_h and is inversely proportional to \sqrt{r} , with:

$$r = \frac{I}{\langle I \rangle} \quad (2)$$

being the ratio of speckle intensity to the mean intensity of the speckle field.



(a) Section 5 with the fit parameter $M = 1.2$



(b) Section 8 with the fit parameter $M = 0.81$

FIG. 2: The distribution of the ratio r of individual speckle intensity to the mean intensity in a speckle field.

The distribution of r for polychromatic sources has also been theoretically estimated and validated using simulations¹⁻³. Over a planar speckle field, the value for r is shown to follow a gamma distribution^{1,3}:

$$p(r) = \frac{M^M r^{M-1}}{\Gamma(M)} \exp(-Mr) \quad (3)$$

The statistics of the measured data can be fitted well using this gamma distribution with a fitting parameter M . As an estimate for the relative intensity of the reflected light the V_{pp}^2 of the photodiode signal was used.

The scan in Fig. 1 was used to evaluate the surface roughness and its effects on precision. Nine planar surfaces were analyzed separately. For each section the mean intensity was calculated, and a gamma distribution was fitted to estimate the probability density function of $r = \frac{I}{\langle I \rangle}$. Two examples of the distribution and the fit are shown in Fig. 2 for a machined section 5 and a non-machined section 8.

We call the ratio between the surface roughness σ_h and the expectation value $\langle \delta z \rangle$ for the measurement uncertainty α . Using the gamma distribution fit and the eq. (1), an expectation value of the measurement uncertainty

$$\langle \delta z \rangle = \alpha \cdot \sigma_h \quad (4)$$

can be calculated.

After finding the value for α and calculating the standard deviation σ_z of the measured surface profile for each of the nine selected planar sections, the rms surface roughness σ_h and the expected uncertainty can be estimated using

$$\sigma_z^2 = \sigma_h^2 + \langle \delta z \rangle^2. \quad (5)$$

The results are shown in the table below:

	Section								
	1	2	3	4	5	6	7	8	9
M	1.2	1.17	1.16	1.22	1.2	1.19	1.15	0.81	0.78
α	1.06	1.07	1.08	1.05	1.05	1.06	1.06	1.41	1.46
σ_z , [μm]	7.6	7.6	7.4	7.6	7.2	7.2	7.1	5.4	4.1
σ_h , [μm]	5.2	5.2	5.0	5.2	4.9	4.9	4.9	3.1	2.3
$\langle \delta z \rangle$, [μm]	5.5	5.6	5.4	5.5	5.2	5.2	5.2	4.4	3.4

TABLE I: rms surface roughness σ_h and expected speckle induced error $\langle \delta z \rangle$ estimations for sections 1-9 in Fig. 1

The relation of speckle induced measurement uncertainty and the surface roughness can also be numerically estimated.

The parameter M in the gamma distribution is estimated to be^{1,3}

$$M = \sqrt{1 + \left(\frac{\sigma_h}{l_c}\right)^2} \quad (6)$$

in case of a Gaussian spectrum where l_c is the coherence length. For a soliton pulse similar behavior is expected, possibly with some prefactor before $\left(\frac{\sigma_h}{l_c}\right)^2$. Using this, we can numerically calculate the dependence between $\frac{\sigma_h}{l_c}$ and $\frac{\langle \delta z \rangle}{l_c}$, shown in Fig. 3. We see that they are approximately on the same scale, which can also be observed in Table I.

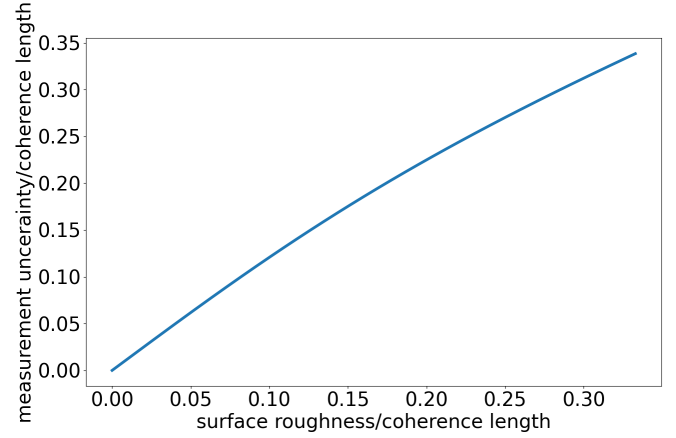


FIG. 3: Numerically calculated dependence of speckle induced measurement uncertainty from the surface roughness in units of the coherence length of the laser source.

However, the theoretical model discussed above is only valid for the range where the surface roughness covers multiple wavelengths of the light source used and does not exceed 1/4 of the coherence length of the optical bandwidth. We already see some discrepancy for non-machined sections 8 and 9 for which the surface roughness is too close to the wavelength. According to eq. (6) the fitting parameter M must be greater than 1, however, for sections 8 and 9 it is smaller.

¹G. Parry, *Laser Speckle and Related Phenomena*, edited by J. C. Dainty, Topics in Applied Physics, Vol. 9 (Springer Berlin Heidelberg, Berlin, Heidelberg, 1975) Chap. 3.1, pp. 78–102.

²P. Pavliček and J. Soubusta, “Theoretical measurement uncertainty of white-light interferometry on rough surfaces,” *Applied Optics* **42**, 1809 (2003).

³P. Pavliček and O. Hýbl, “White-light interferometry on rough surfaces—measurement uncertainty caused by surface roughness,” *Applied Optics* **47**, 2941 (2008).

⁴E. Baumann, J.-D. Deschênes, F. R. Giorgetta, W. C. Swann, I. Coddington, and N. R. Newbury, “Speckle phase noise in coherent laser ranging: fundamental precision limitations,” *Optics Letters* **39**, 4776 (2014).